


Article

Corrosion Behavior of Al₂O₃-40TiO₂ Coating Deposited on 20MnNiMo Steel via Atmospheric Plasma Spraying in Hydrogen Sulfide Seawater Stress Environments

Xian Zeng ^{1,*}, Xiangxiang Chen ¹, Yongjun Wang ², Hao Zhang ² , Qian Cao ¹ and Xudong Cheng ¹¹ School of Materials Science and Engineering, Wuhan University of Technology, Wuhan 430070, China² China Ship Scientific Research Center, Wuxi 214000, China

* Correspondence: zengxian@whut.edu.cn

Abstract: In this study, an Al₂O₃-40TiO₂ coating was deposited on 20MnNiMo steel via atmospheric plasma spraying. The corrosion behavior of the coating was investigated in both artificial seawater and a simulated environment with hydrogen sulfide and high pressure. Additionally, ion dissolution experiments were conducted to evaluate the coating's bio-friendliness. In artificial seawater, the corrosion rate (based on the corrosion current) of the Al₂O₃-40TiO₂ coating initially decreased before increasing. It was speculated that the blocking of corrosion products in the defect channels was helpful in delaying the progress of corrosion in the early stage. The coating had a corrosion current on the order of 10⁻⁶ A/cm² in artificial seawater, suggesting good protection in conventional seawater environments. In the simulated environment, the corrosion rate (based on the weight loss) of the Al₂O₃-40TiO₂ coating showed a continuously declining trend. It was deduced that, unlike corrosion products in artificial seawater, the corrosion products in the simulated environment (e.g., metal sulfide) might be more chemically stable, leading to a longer blocking effect. Therefore, a minimal corrosion rate of 0.0030 mm/a was obtained after the coating was immersed for 30 days. The amount of dissolved coated elements was negligible and there were only small amounts of dissolved non-coated elements such as Ni and Mo. The developed coating can be considered to be highly biofriendly if the non-coated area of the specimen is well sealed.

Keywords: Al₂O₃-40TiO₂ ceramic coating; corrosion behavior; hydrogen sulfide seawater; ion dissolution experiment; APS method



Citation: Zeng, X.; Chen, X.; Wang, Y.; Zhang, H.; Cao, Q.; Cheng, X. Corrosion Behavior of Al₂O₃-40TiO₂ Coating Deposited on 20MnNiMo Steel via Atmospheric Plasma Spraying in Hydrogen Sulfide Seawater Stress Environments. *Coatings* **2024**, *14*, 588. <https://doi.org/10.3390/coatings14050588>

Academic Editors: Henryk Kania, Florence Lequien and Anzelina Marek

Received: 16 April 2024

Revised: 3 May 2024

Accepted: 6 May 2024

Published: 8 May 2024



Copyright: © 2024 by the authors. Licensee MDPI, Basel, Switzerland. This article is an open access article distributed under the terms and conditions of the Creative Commons Attribution (CC BY) license (<https://creativecommons.org/licenses/by/4.0/>).

1. Introduction

Combustible ice, also known as a natural gas hydrate, has a high combustion value, abundant reserves, low pollution emission, and high energy density. Due to the intensification of the world's energy crisis, combustible ice is attracting increasing attention as a new clean energy source. It is primarily found in seafloor sediments and permafrost, whose current proven reserves are as high as 3000 trillion cubic meters, making it a promising resource for exploitation; combustible ice has been hailed as 'the energy of the future' [1,2]. However, the mining equipment of deep-sea combustible ice faces high-pressure environments and corrosion from hydrogen sulfide seawater. Furthermore, the decomposition of combustible ice releases fluids rich in methane and hydrogen sulfide, which promotes the existence of unique ecosystems (cold seeps) that use these chemical compounds as a source of energy. These ecosystems rely on chemoautotrophic bacteria as primary producers for community structure reproduction [3,4]. Therefore, the bio-friendliness of equipment materials must be addressed [5]. Applying a biofriendly and corrosion-resistant coating to mining equipment of combustible ice is often suggested as an effective and economical way of protecting such equipment [6].

Generally, anticorrosive coatings used in marine environments can be divided into three categories—namely, organic, metallic, and ceramic coatings—depending on the nature

of the coating materials. Organic coatings may swell and fail under high pressure and metallic coatings may spill metal ions, which can have an impact on the environment. In comparison, ceramic coatings are more chemically stable and biofriendly [7–9]. Among the existing coating methods, atmospheric plasma spraying (APS) is widely used due to its flexible processability and broad material availability. In particular, Al_2O_3 -based ceramic coatings deposited by the APS method are commonly used in marine environments due to their effective shielding protection and stability. However, a pure Al_2O_3 coating has some disadvantages. Its plasticity is poor, making it prone to cracking and flaking during assembly and maintenance, which reduces its durability and reliability [10]. To address this issue, TiO_2 is typically added to the original Al_2O_3 powder as a second phase. The melting point of TiO_2 (1850 °C) is lower than that of Al_2O_3 (2054 °C), resulting in good wettability. This property is beneficial during the coating formation process as it facilitates the filling and sealing of pores. TiO_2 has greater toughness than Al_2O_3 , which helps to prevent the formation of cracks in the coating. TiO_2 is highly stable and does not readily undergo chemical reactions, making it highly corrosion-resistant. The addition of TiO_2 helps to seal holes, release stress, reduce cracks, and improve the toughness, corrosion resistance, and overall mechanical properties of coatings [11]. Toma et al. found that the addition of TiO_2 to Al_2O_3 improved the corrosion stability of coatings [12]. Al_2O_3 -40 TiO_2 coatings have considerable application potential in the field of surface protection. Kumar et al. confirmed the protective effect of Al_2O_3 - TiO_2 coating on a substrate in a 3.5% NaCl solution [13]. Jiang et al. investigated the long-term corrosion resistance of atmospheric plasma-sprayed Al_2O_3 -40 TiO_2 coatings in NaCl solution. They found that these coatings maintained good protection even after 70 days of immersion time [14]. Wei et al. investigated the corrosion performance of a plasma-sprayed Al_2O_3 -40 TiO_2 coating in sulfur-containing NaCl solution and also confirmed the good effect of the coating [15].

However, most of the abovementioned studies focused only on the properties of coatings with Al_2O_3 -40 TiO_2 in conventional aqueous environments. The corrosion behavior of Al_2O_3 -40 TiO_2 coatings in harsh seawater environments with high pressure and wet hydrogen sulfide has not yet been studied. Thus, in this study, commercially available Al_2O_3 -40 TiO_2 ceramic powders were purchased and processed for coating via atmospheric plasma spraying. The corrosion behavior of the Al_2O_3 -40 TiO_2 coating in artificial seawater and simulated high-pressure seawater with wet hydrogen sulfide was investigated. The microstructure, phase compositions, and electrochemical properties of the coating before and after the corrosion test were characterized to explore the corrosion mechanism. Ion dissolution experiments were carried out to assess the bio-friendliness of the coating. The study results may offer insights into the long-term corrosion resistance of mechanical components operating in deep-sea environments containing wet hydrogen sulfide.

2. Materials and Methods

2.1. Original Materials and Preparation Methods

Commercially available Al_2O_3 -40 TiO_2 powders (45–90 μm , Pilot (Yiyang) Plasma Powder Co., Ltd., Yiyang, China) were used as the coating materials. 20MnNiMo steel served as the substrate and its specific composition is shown in Table 1. Prior to spraying, the substrate was degreased and cleaned with acetone and then sandblasted to enhance surface roughness and promote adhesion to the coating. The grit-blasted process used brown corundum sand with a grain size of 0.18 mm (80#), a pressure of 0.35–0.4 MPa, a blasting distance of 30–50 mm, and a blasting angle of 75°–90° to the surface of the workpiece. The surface of the sandblasted workpiece was visually observed to be uniformly rough and dull. The coating was deposited using an APS-3000 thermal spraying system (Beijing Institute of Aerospace Manufacturing Technology, Beijing, China) equipped with an ABB industrial robot (IRB2400-16, ABB, Västerås, Sweden). Before the deposition of the ceramic layer, a corrosion-resistant NiCrMo (45–90 μm , Zhenxing (Chengdu) Metal Powder Co., Ltd., Chengdu, China) bonding layer was deposited to improve the bond strength of the overall coating, as well as to weaken the difference in the coefficient of thermal

expansion between the ceramic layer and the substrate, thereby reducing the spray thermal stress of the coating. When preparing the coating, the spray path and spray distance were determined according to the sample size and coating requirements and the program was set up accordingly. The spray parameters were set up, with preheating before feeding the powder, according to the thickness of the coating to determine whether the spraying was complete. The spraying of the NiCrMo bonding layer and Al₂O₃-40TiO₂ coating was conducted under the optimum spray parameters presented in Table 2.

Table 1. Specific composition of the base material 20MnNiMo (wt%).

Element	C	Si	Mn	Cr	Mo	Ni	P	S	Al	Fe
Content	0.17–0.23	0.20–0.35	0.40–0.70	0.35–0.65	0.20–0.70	1.60–2.20	≤0.030	≤0.030	0.20–0.30	Bal.

Table 2. Plasma spraying process parameters.

Process Parameters	Bonding Layer	Ceramic Layer
Current/A	400	500
Voltage/V	68–70	77–79
Plasma gas flow (Ar)/L·min ⁻¹	40	30
Plasma gas flow (H ₂)/L·min ⁻¹	1	6.5
Plasma gas flow (N ₂)/L·min ⁻¹	1	1
Powder gas flow (N ₂)/L·min ⁻¹	5	5
Spray distance/mm	130	90
Powder feed rate/g·min ⁻¹	25	22
Spray gun speed/mm·s ⁻¹	500	300

2.2. Test and Characterization Methods

2.2.1. Corrosion Behavior of Coating in Artificial Seawater

The corrosion behavior of the coating after 28 days of immersion in artificial seawater was evaluated using the electrochemical technique of the CS electrochemical workstation (CS2350, Wuhan Kote Instrument Co., Ltd., Wuhan, China). The artificial seawater was configured with specific components, as shown in Table 3 [16]. The test specimen for electrochemical analysis was prepared by cutting it into samples with a size of 1 cm × 1 cm, grinding and polishing the back side, and connecting the samples to a copper wire. Then, the samples were placed in a mold and set in resin. The coated area was left as the test part, with the copper wire connected to the substrate at one end and the electrochemical workstation at the other end. The samples were placed in a room-temperature solution, which was replaced every 7 days to maintain the freshness of the solution. All beakers containing the samples and solution were sealed to avoid the evaporation of water. The electrochemical experiments were conducted using a three-electrode system. The coating specimen served as the working electrode, the platinum sheet as the counter electrode, and the saturated calomel electrode (SCE) as the reference electrode. Under the premise of a stable open-circuit potential, the electrochemical impedance spectroscopy (EIS) measurements were conducted in the frequency range of 10⁻² Hz to 10⁵ Hz at an alternating current amplitude of 10 mV. The impedance spectra were analyzed using the Zview (version number: ZView 3.1c) and ZsimpWin (version number: ZsimpWin 3.3) commercial software. The dynamic potential polarization was tested at a scanning speed of 0.5 mV·s⁻¹. Tafel plots were constructed to calculate the corrosion potential (E_{corr}) and corrosion current density (i_{corr}). All electrochemical tests were repeated at least three consecutive times to ensure the reproducibility of the measurement results.

Table 3. Composition of artificial seawater.

Compound	Concentration (g/L)
NaCl	24.53
MgCl ₂	5.20
Na ₂ SO ₄	4.09
CaCl ₂	1.16
KCl	0.70
NaHCO ₃	0.20
KBr	0.10
H ₃ BO ₃	0.03
SrCl ₂ ·6H ₂ O	0.03

2.2.2. Corrosion Behavior of Coating in a Simulated High-Pressure Seawater Environment with Wet Hydrogen Sulfide

To simulate a high-pressure seawater environment with wet hydrogen sulfide, the experiment was carried out with the setup shown in Figure 1. High-purity N₂ was continuously fed into the reaction vessel to remove the air trapped inside during installation. An H₂S/N₂ gas mixture with an H₂S concentration of 50 mg/L was then continuously fed to maintain a stable H₂S concentration throughout the test cycle. The experimental basic solution was artificially configured seawater with a hydrogen sulfide concentration of 50 mg/L. The specimens were subjected to a bending load to satisfy the pressure condition of 450 MPa. Figure 2 shows a physical image of the fixture. The specimens (60 mm × 10 mm × 2 mm) used in this part of the experiment were spray-coated on all six sides and then sealed with an organosilicon sealer [17]. The samples were taken out on days 10, 20, and 30 for measurement; their morphological and physical changes were detected and the corrosion products were removed from the surface of the specimens using an acid wash solution (composition: 150 mL of hydrochloric acid ($\rho = 1.19$ g/mL) and distilled water to form a 1000 mL solution), rinsed with deionized water, dehydrated with anhydrous ethanol, blown dry in cold air, and measured for weight. The corrosion rate was determined using the weight loss method and calculated according to Equation (1):

$$V_{CR} = \frac{8.76 \times 10^4 \Delta W}{S \rho t} \quad (1)$$

where V_{CR} is the corrosion rate (mm/y), ΔW is the difference in weight before and after corrosion (g), S is the area of the sample (cm²), ρ is the density of the sample (g/cm³), and t is the immersion time (h).

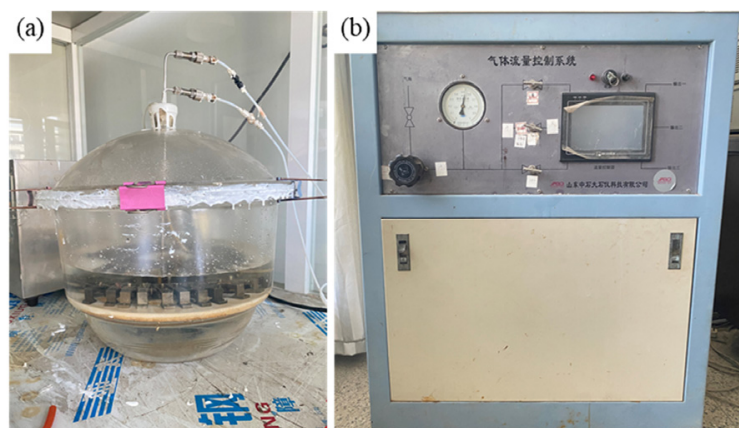
**Figure 1.** Stress corrosion test setup: (a) reaction vessel and (b) gas flow control system.



Figure 2. Four-point bending method with stress loading: physical image of the fixture.

2.2.3. Ion Leaching Behavior of Coating in Ultrapure Water

Ion dissolution experiments were performed to evaluate the bio-friendliness of the coating. The experiments were conducted at room temperature using ultrapure water as the dissolution medium. The volume of ultrapure water was determined according to Equation (2). The coated side of each specimen was sealed with the coating, while the other sides were sealed with fluorocarbon resin. The specimen was placed in a sealable PE canister and then the corresponding volume of ultrapure water was added. Thus, the immersion process was carried out in a sealed environment. After completing one cycle of immersion, a disposable dropper was used to extract a certain volume of water for testing. The remaining water was discarded and a new corresponding volume of ultrapure water was added for the next immersion cycle. Cycles 1, 2, and 3 each lasted seven days. Cycle 4 lasted 14 days and cycles 5, 6, and 7 each lasted 28 days, totaling 119 days. Equation (3) was used to calculate the dissolution rate of each metal particle in the leaching solution, as determined by inductively coupled plasma mass spectrometry.

$$V = 200A \quad (2)$$

$$Vp = \frac{Cp}{T} \quad (3)$$

where V is the volume of ultrapure water (L), A is the area of the coating region (m^2), Vp is the dissolution rate of metal ions ($\mu\text{g}\cdot\text{L}^{-1}\cdot\text{d}^{-1}$), Cp is the dissolved concentration of metal ions measured in the test ($\mu\text{g}\cdot\text{L}^{-1}$), and T is the immersion time (day).

In addition, to verify that the ion-dissolved elements originated from the unclosed side of the matrix, a verification experiment of ion dissolution was conducted. The specimens' test surfaces were all spray-coated and sealed to eliminate the influence of the substrate side. A control group that was not coated before immersion in ultrapure water was simultaneously set up to compare the experimental results. The specimens for the validation experiment were immersed over 2 cycles of 7 days each.

2.2.4. Microstructural Characterization and Phase Analysis

The phase composition of the coating before and after corrosion was analyzed by using an X-ray diffractometer (X-ray D8 Advance, Bruker Corporation, Billerica, MA, USA) using Cu $K\alpha$ radiation ($\lambda = 1.54056 \text{ \AA}$) with a step size of 0.02° . The morphological changes in the coating before and after immersion were observed using a Scanning Electron Microscope in backscatter mode (BSE) (SEM, JSM-IT800, Japan Electronics Co., Ltd, Tokyo, Japan). Based on the SEM images, the chemical composition of the coating before and after immersion was analyzed using an Energy-Dispersive Spectrometer (EDS, Ultim max 65, Oxford Instruments, Abingdon, UK). The porosity of the coating was determined from the SEM images of randomly selected cross-sectional areas at $300\times$ magnification using the Image J software (version number: Image J 1.52) and the average values were calculated and analyzed.

3. Results and Discussion

3.1. Characterization of $\text{Al}_2\text{O}_3\text{-40TiO}_2$ Coating before Corrosion

Figure 3a,b shows the surface morphology of the $\text{Al}_2\text{O}_3\text{-40TiO}_2$ coating. The molten and semi-molten powder particles on the surface are clearly visible. Porosity and cracks were also observed, which are common defects of plasma-sprayed ceramic coatings [18,19]. Figure 3c displays the cross-sectional morphology of the coating, revealing a three-layer structure of ceramic layer–bonding layer–substrate; however, in Figure 3d, some pits can also be observed inside the coating. The porosity of the coating was approximately 2.57%, which served as a channel for the corrosive liquid to penetrate the coating and ultimately affect its corrosion resistance.

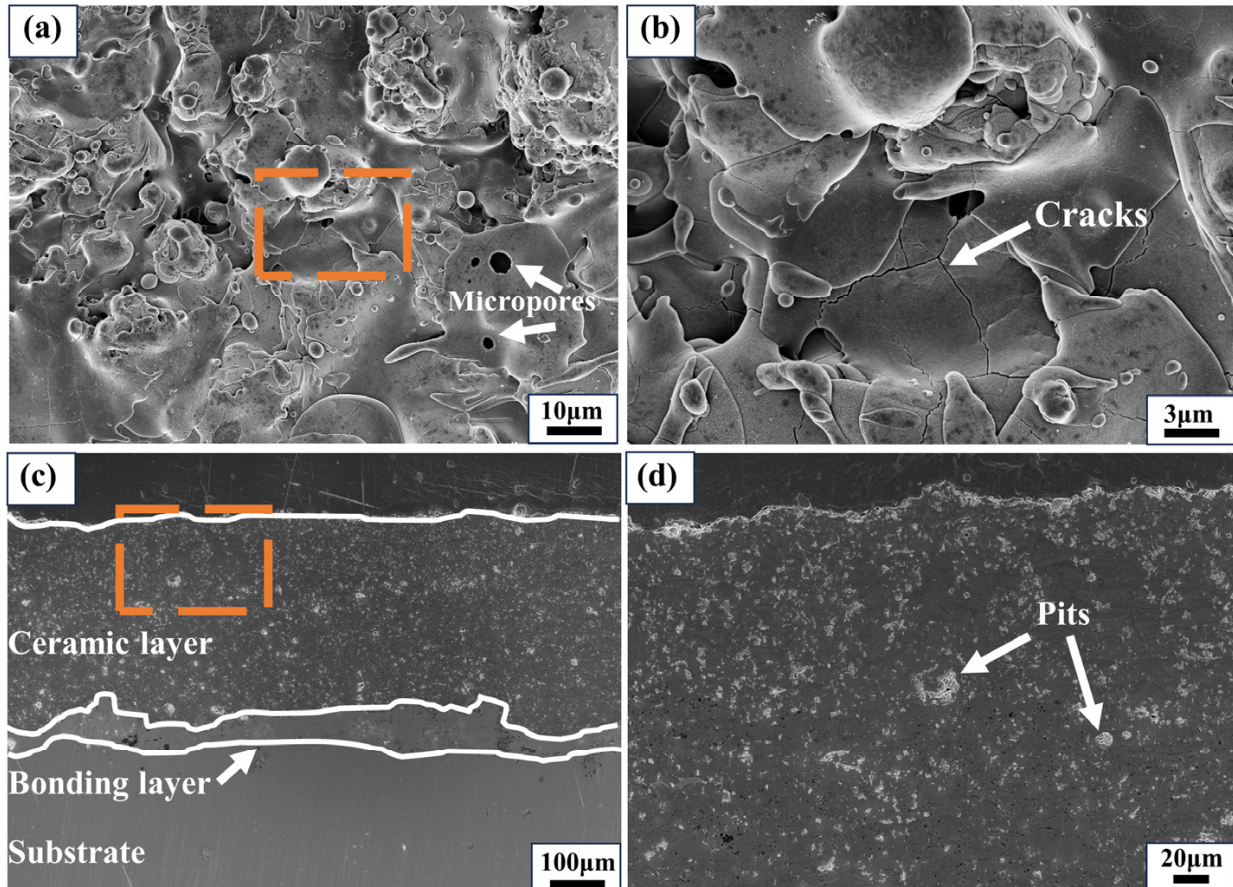


Figure 3. SEM images of $\text{Al}_2\text{O}_3\text{-40TiO}_2$ coating: (a,b) surface and (c,d) cross-section. (Figure (b) is an enlarged view of the orange area in Figure (a), Figure (d) is an enlarged view of the orange area in Figure (c)).

Figure 4 shows the XRD patterns of the $\text{Al}_2\text{O}_3\text{-40TiO}_2$ powder and deposited coating. It was observed that the XRD pattern of the powder mainly contains the peaks of $\alpha\text{-Al}_2\text{O}_3$ and rutile TiO_2 , along with the detected peaks of Al_2TiO_5 . This could be attributed to the sintering process during powder preparation. Ti^{4+} , which has a larger ionic radius than Al^{3+} , is more likely to occupy the interstitial sites of the alumina lattice and form the Al_2TiO_5 phase [20]. The $\gamma\text{-Al}_2\text{O}_3$ phase was observed in the sprayed coating. Therefore, the coating preserved the $\alpha\text{-Al}_2\text{O}_3$ phase during solidification by using incompletely melted $\alpha\text{-Al}_2\text{O}_3$ particles as the nucleation points. Simultaneously, the lower free energy of nucleation made it easier for $\gamma\text{-Al}_2\text{O}_3$ to form during cooling, resulting in the creation of the $\gamma\text{-Al}_2\text{O}_3$ phase [21].

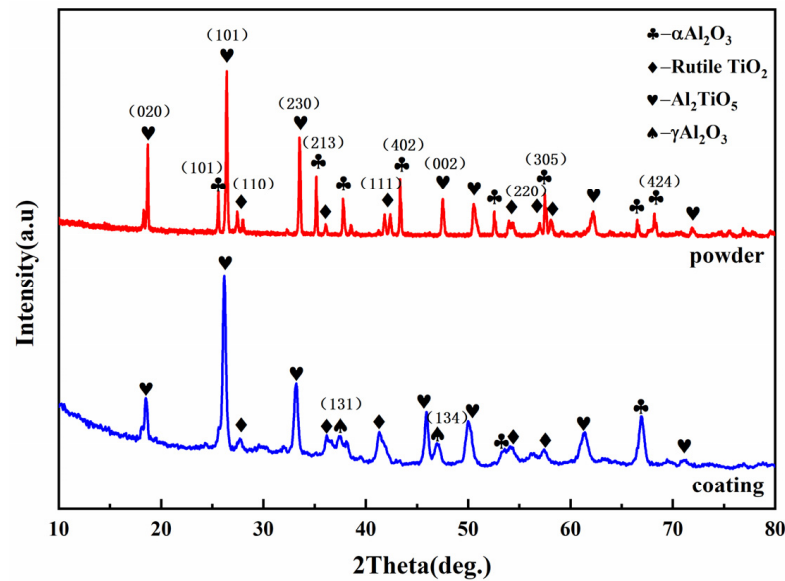


Figure 4. XRD patterns of Al_2O_3 -40 TiO_2 powder and coating.

3.2. Corrosion Behavior of Coating in Artificial Seawater

Figure 5 displays the polarization curves of the Al_2O_3 -40 TiO_2 coating at various immersion time points and of the unimpregnated substrate and Table 4 presents the corresponding curve fitting data. It is evident that the corrosion potential (E_{corr}) of the substrate was at its minimum value without immersion. Generally, a smaller corrosion potential indicates a larger corrosion resistance tendency. The larger corrosion tendency of the coating immersed for 0 days might be related to the initial defects present in it, such as pores and cracks. These defects increased the true surface area exposed to the electrolyte, which affected the corrosion susceptibility [22]. Additionally, they allowed the corrosive fluid to access the substrate via the inside of the coating. As the immersion time increased, the coating's corrosion potential first increased and then decreased. This might be related to the growth and dissolution of corrosion products. During the first 14 days of immersion, the corrosive fluid corroded the substrate through coating defects. Then, the generated corrosion products filled the defective channels, preventing the corrosive fluid from entering and reducing the tendency to corrode [12]. With a longer immersion time, the corrosion products dissolved, weakening the filling of coating defects. The corrosion potential (E_{corr}) gradually reduced but still remained higher than that on 0 days of immersion. The coating exhibited the smallest corrosion current density (i_{corr}) on the 14th day, which corresponded well to the corrosion potential. The corrosion currents on the other days changed by an order of 10^{-6} $\text{A}\cdot\text{cm}^{-2}$ and were all lower than the corrosion current of the substrate, indicating that the coating exerted a good protective effect on the substrate in the artificial seawater.

Table 4. E_{corr} and i_{corr} values of the coating and substrate at different immersion time points (reference electrode: SCE).

Time (d)	E_{corr} (V)	i_{corr} (A/cm^2)	β_a ($\text{mV}\cdot\text{decade}^{-1}$)	β_c ($\text{mV}\cdot\text{decade}^{-1}$)
0 (substrate)	−0.748	1.013×10^{-5}	70.731	−236.64
0 (coating)	−0.615	3.406×10^{-6}	129.27	−94.33
14 (coating)	−0.503	2.450×10^{-6}	156.05	−125.98
28 (coating)	−0.525	3.653×10^{-6}	141.49	−119.83

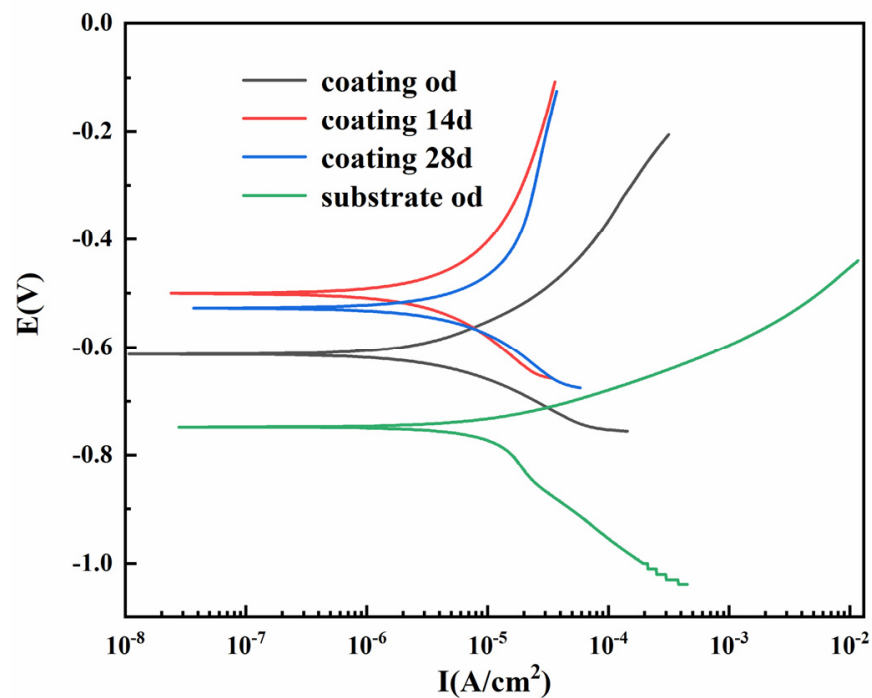


Figure 5. Dynamic potential polarization curves of the coating at different immersion time points and of the non-impregnated substrate (reference electrode: SCE).

EIS is a suitable method to simulate electrochemical reactions at the metal–solution interface and characterize the corrosion stability of coatings. The corrosion resistance of the coating was evaluated after immersion via electrochemical impedance spectroscopy (EIS). The Nyquist plot and Bode plots (frequency–mode and frequency–phase angle) are shown in Figure 6. It was observed that after 14 days of immersion, the coating had the largest tolerable arc diameter and modal value in the low-frequency band, indicating the best corrosion resistance [23]. Moreover, it is evident that the curves of both Bode plots exhibit two time constants. This suggests that corrosion took place at the interface between the coating and the substrate, where a double electric layer was formed [24]. Based on this information, the AC impedance data were fitted using the Zview software and an equivalent circuit was constructed, as shown in Figure 7, where R_{pore} , R_{ct} , Q_{c} , and Q_{dl} represent the pore resistance, charge-transfer resistance, capacitance of the coating, and double-layer capacitance, respectively. Weber’s impedance (Z_{w}) is often used to indicate diffusion processes and corrosion products adhering to a coating [25]. The results suggested that the coating might be unstable under long-term erosion in artificial seawater and that the substances within the coating might have undergone dissolution or corrosion [26,27].

The data obtained after impedance curve fitting are presented in Table 5. When a high-frequency signal was applied to the sample, corrosion resistance was caused by solution resistance (R_{s}). As the frequency decreased, ions and electrons in the solution and coating migrated toward the solid–liquid interface. During this process, corrosion resistance was primarily determined by R_{pore} and R_{ct} , which are the key indicators for evaluating the corrosion resistance of a coating sample [28,29]. The results showed that the coating had the highest R_{pore} and R_{ct} after 14 days of immersion, indicating superior corrosion resistance at that time point. This finding was consistent with the polarization curves.

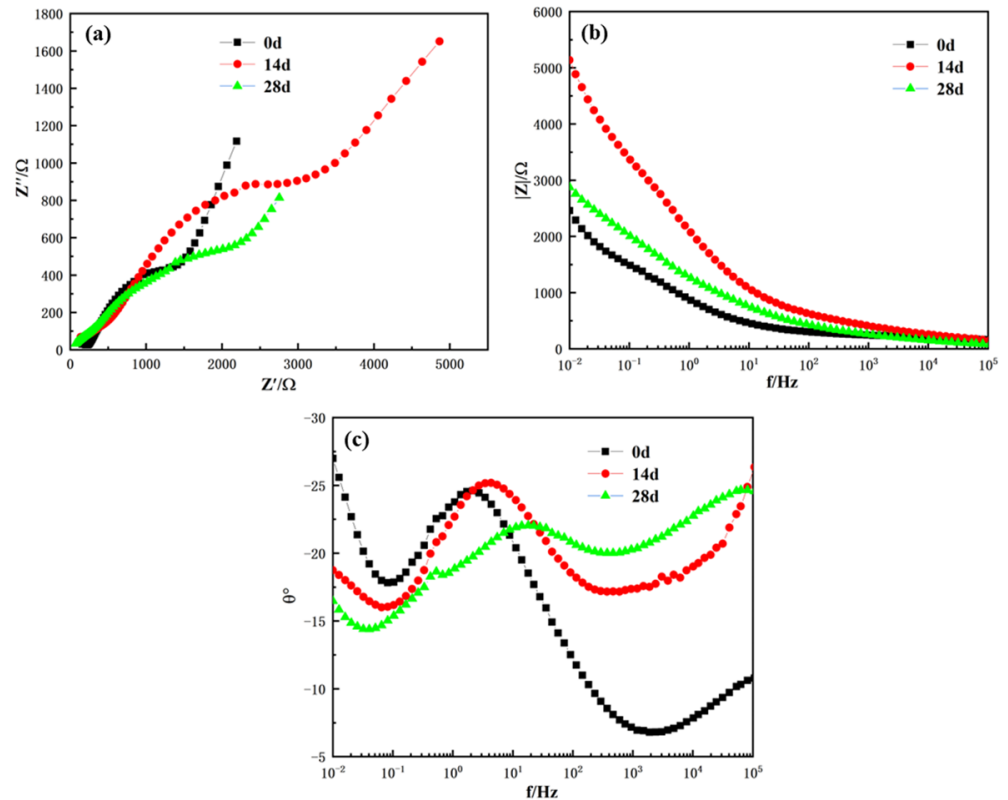


Figure 6. AC impedance spectra of coating on different days of immersion: Nyquist plot (a), Bode impedance magnitude plot (b), and Bode phase angle plot (c) (reference electrode: SCE).

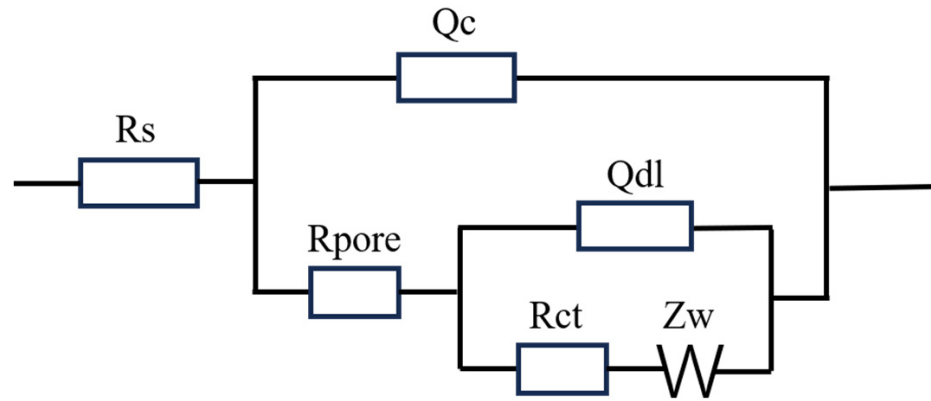


Figure 7. Equivalent circuit fitting model based on EIS graph.

Table 5. The equivalent circuit data of the coating (reference electrode: SCE).

Time (d)	R_s ($\Omega \cdot \text{cm}^2$)	Q_c ($\mu\text{F} \cdot \text{cm}^{-2}$)	n_{coat}	R_{pore} ($\Omega \cdot \text{cm}^2$)	Q_{dl} ($\mu\text{F} \cdot \text{cm}^{-2}$)	n_{dl}	R_{ct} ($\Omega \cdot \text{cm}^2$)	W ($\Omega \cdot \text{cm}^{-2} \cdot \text{s}^{-1/2}$)
0	26.78	5.0552×10^{-5}	0.3511	216.4	4.3075×10^{-4}	0.5142	1980	2.682×10^{-3}
14	20.71	6.6334×10^{-5}	0.2722	667.1	1.5731×10^{-4}	0.4911	4341	1.873×10^{-3}
28	20.93	1.0245×10^{-4}	0.3603	538.6	2.7932×10^{-4}	0.3682	2852	1.195×10^{-3}

3.3. Corrosion Behavior of Coating in a Simulated High-Pressure Seawater Environment with Wet Hydrogen Sulfide

Figure 8 shows the macroscopic morphology of the coating surface after different immersion times in the simulated seawater environment. It was found that most of the coating surface had no visible signs of corrosion, except for some brown rust in the edge area. In addition, when prolonging the immersion time to 30 days, cracks appeared in

the edge area and then extended to the middle area of the surface. An SEM morphology analysis was conducted on the uncracked and cracked areas of the coating sample after 30 days of immersion and the results are presented in Figures 9 and 10, respectively.

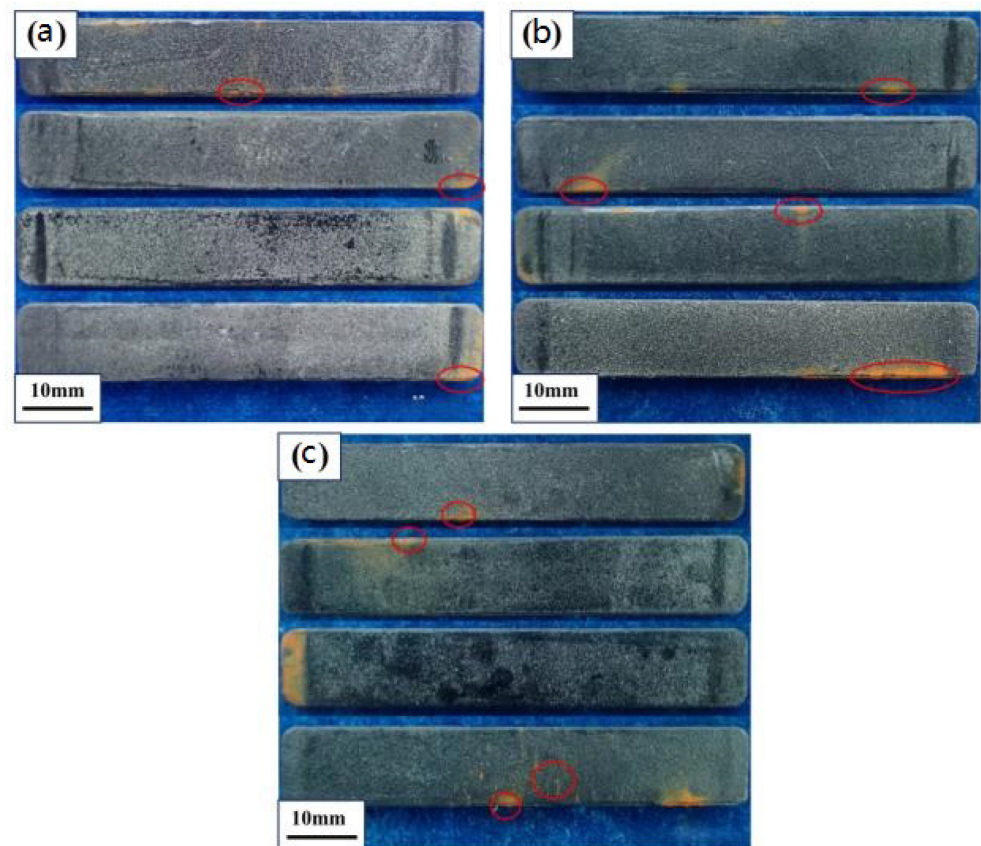
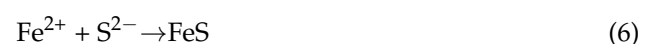


Figure 8. Macroscopic morphology of coating after (a) 10 days, (b) 20 days, and (c) 30 days of immersion. (The red circle in the figure represents the areas where edge corrosion occurs in the coating under different corrosion days).

In the uncracked area shown in Figure 9, the distribution of Si was in contrast with that of Al and Ti, suggesting that the sealant covered the ceramic coating incompletely. Furthermore, a low concentration of Fe was detected in the EDS analysis, which was barely changed from that of the original coating, as shown in Table 6. However, in the cracked area shown in Figure 10, there was an enrichment of Fe and S, demonstrating that severe corrosion of the substrate occurred. The corrosion mechanism of steel caused by wet hydrogen sulfide can be summarized as follows: hydrogen sulfide dissolves in water and undergoes an ionization reaction, producing H^+ and S^{2-} . H^+ is then reduced to hydrogen after the capture of the electrons on the surface of the steel workpiece, according to Equation (4). Subsequently, steel (Fe) loses electrons to form Fe^{2+} and reacts with S^{2-} to form FeS, according to Equations (5) and (6), respectively [30–32]. Moreover, Fe^{2+} is unstable and readily oxidizes to Fe^{3+} , forming iron oxides and hydroxides.



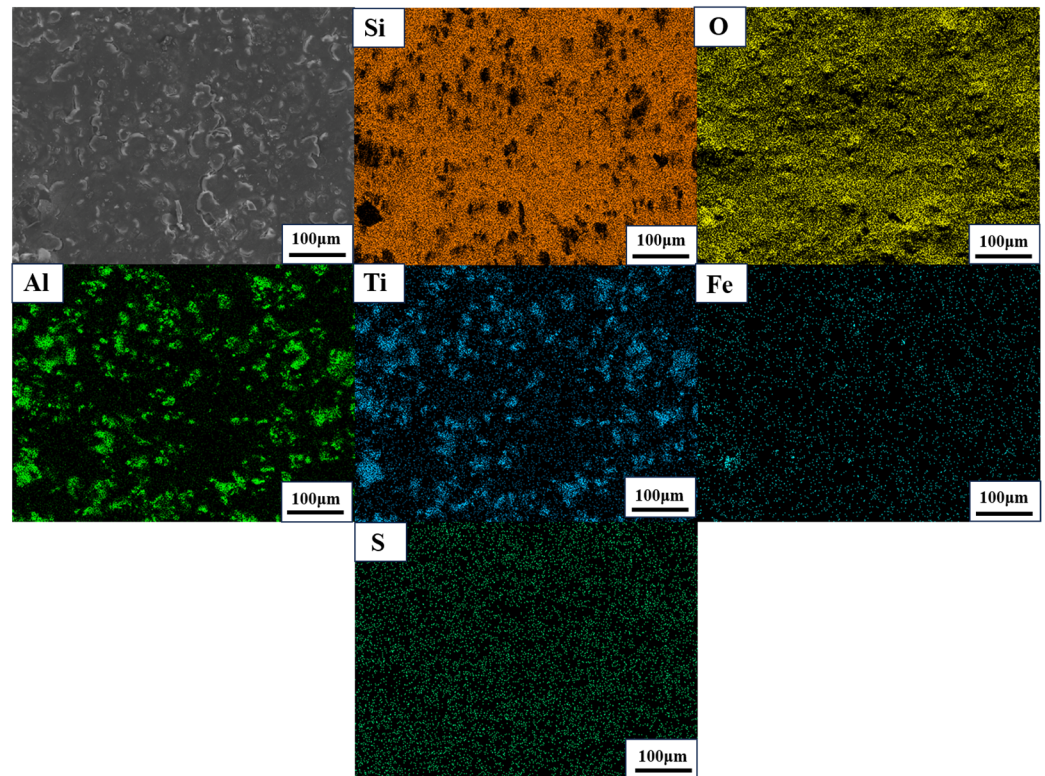


Figure 9. Morphology and elemental distribution of an uncracked area after 30 days of immersion (the elements include sealer elements (Si and O) and coating material elements (Al and Ti), as well as Fe and S).

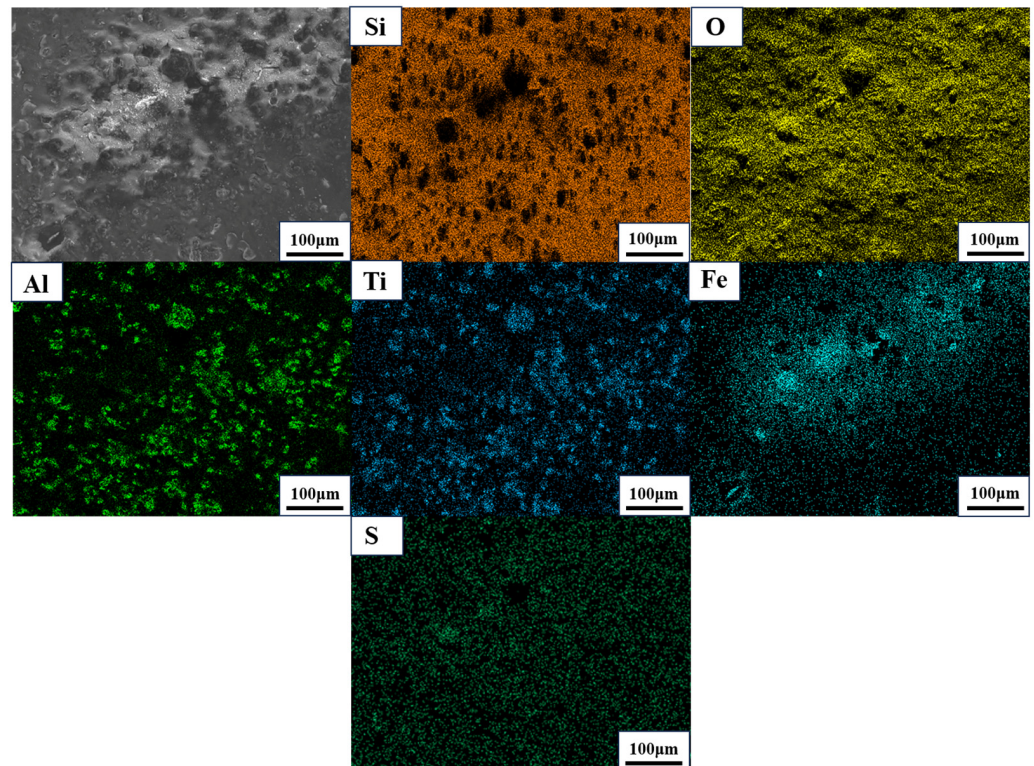


Figure 10. Morphology and elemental distribution of a cracked area after 30 days of immersion (the elements include sealer elements (Si and O) and coating material elements (Al and Ti), as well as Fe and S).

Figure 11 shows the XRD patterns of the $\text{Al}_2\text{O}_3\text{-40TiO}_2$ coating before and after corrosion in the simulated environment. As there was a very small concentration of Fe and S on the coating surface, their related corrosion products were not detected in the XRD analysis, which showed an almost unchanged diffraction pattern. Figure 12 shows the corrosion rate of the $\text{Al}_2\text{O}_3\text{-40TiO}_2$ coating versus immersion time in the simulated environment. Numerically, the corrosion rate of the coating decreased with an increase in the immersion time. The minimal corrosion rate of the coating was obtained after 30 days of immersion, which was about 0.0030 mm/a. As we mentioned above, the blocking of corrosion products in defect channels, such as pores and interfaces, hinders the corrosion process, thereby reducing the corrosion rate. The declining corrosion rate of the $\text{Al}_2\text{O}_3\text{-40TiO}_2$ coating in the simulated environment was attributed to the blocking of metal sulfides such as FeS. Chloride ions have a small radius and strong penetration and, in artificial seawater environments, they are able to destroy the oxide film of corrosion products at the interface of the substrate and coating and weaken the protective effect of these products [33,34]. Unlike corrosion products in artificial seawater, corrosion products in a simulated environment might be more chemically stable, leading to a longer blocking effect [14,15]. As a result, the re-increase in corrosion rate due to the dissolution of corrosion products is avoided. In this study, the coating began to crack after 30 days of immersion under the influence of external stress and the expansion stress of corrosion products. It is worth mentioning that cracks arose at the edges of the specimen and extended to the coating surface, which meant that these cracks were more likely to be stress cracks than corrosion cracks. Therefore, sharp corners should be avoided when applying an $\text{Al}_2\text{O}_3\text{-40TiO}_2$ coating as an anti-corrosion coating.

Table 6. Results of EDS surface scanning in different regions (at%).

Elements	C	O	Si	Al	Ti	Fe	S
Original coating	57.6	24.2	16.0	1.0	0.7	0.1	-
Uncracked area	53.8	27.5	15.2	1.9	1.2	0.2	-
Cracked area	48.5	31.3	14.8	2.2	1.3	1.7	0.3

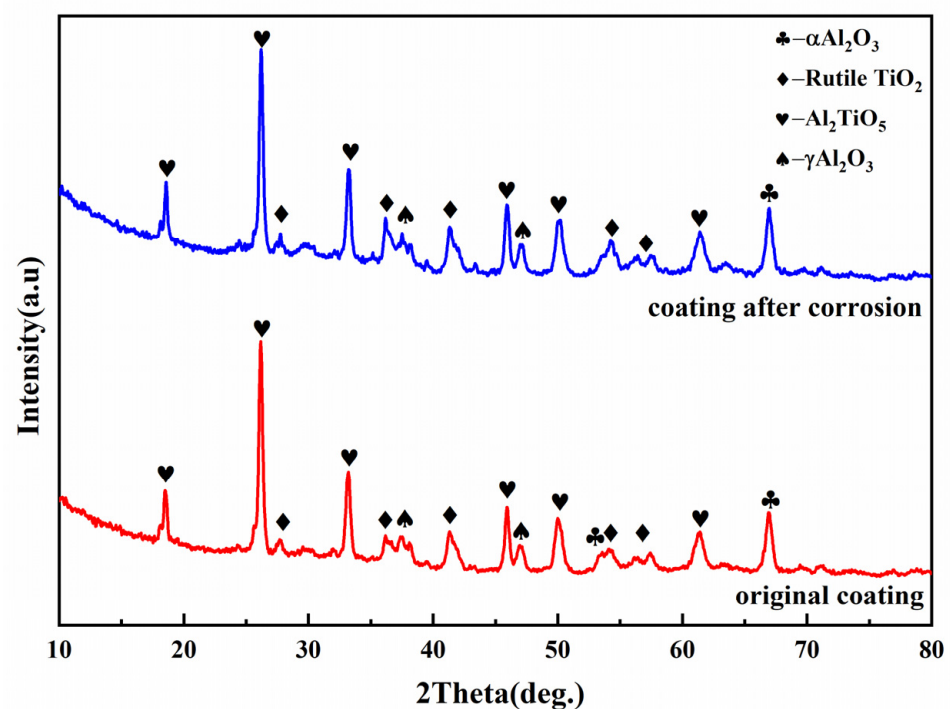


Figure 11. XRD patterns of coating before and after 30 days of immersion in a simulated environment.

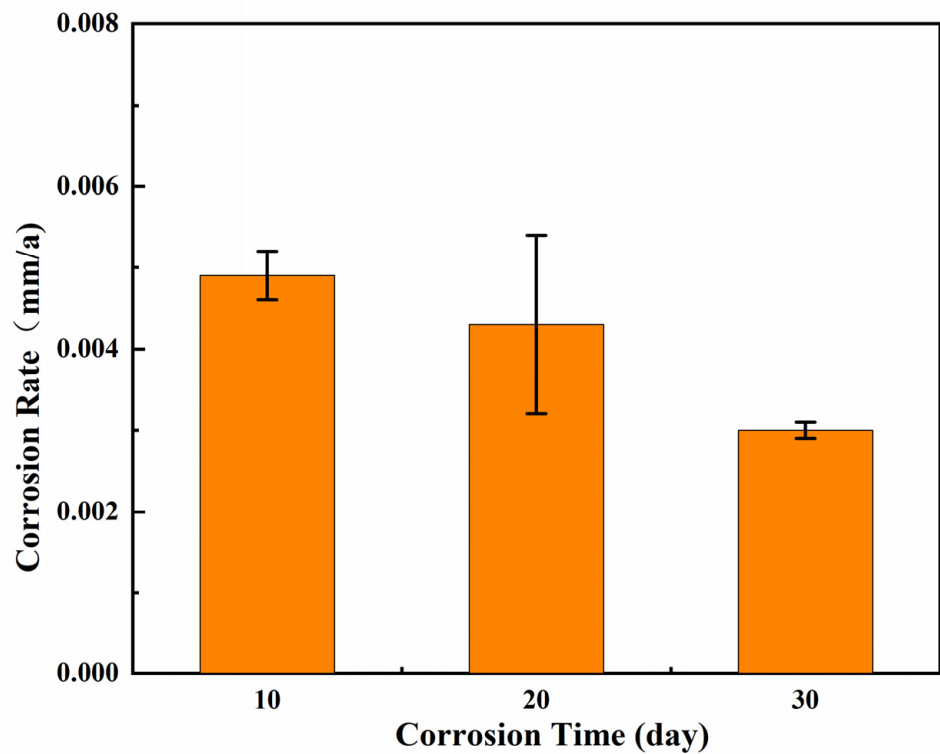


Figure 12. Corrosion rates of the coating at different immersion time points in the simulated environment.

3.4. Results of Ion Dissolution Experiments

Figure 13 shows the average ion dissolution rate of the Al₂O₃-40TiO₂ coating after each test cycle. During the immersion process in ultrapure water, ion dissolution of Ni and Mo was detected. The ion dissolution rate gradually decreased with the prolongation of immersion time. In the seventh cycle, the dissolution rate of Ni was 0.04 μg·L⁻¹·d⁻¹ and that of Mo was 0.01 μg·L⁻¹·d⁻¹. Ni and Mo were detected as non-coated elements, possibly because of the sealing by fluorocarbon resin on the closed side. The ion dissolution concentrations for the remaining elements showed specific values that were below the lower limits of the instrument test. In summary, if the side sealed by fluorocarbon resin is better protected, the area of the coating after sealing has a small potential of ion leaching.

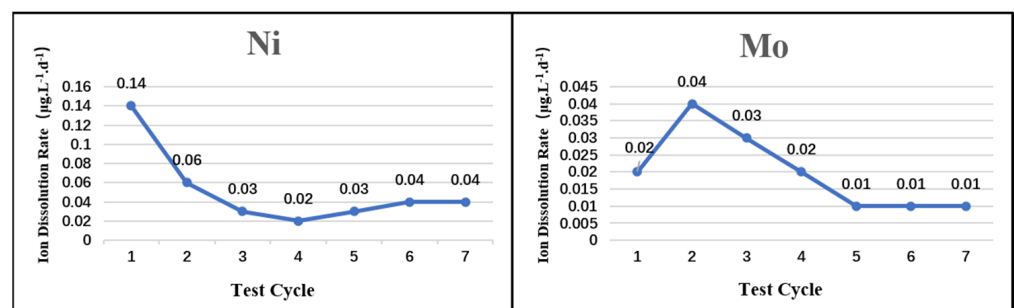


Figure 13. Changes in ion dissolution rate in Al₂O₃-40TiO₂ coating across various cycles of immersion in ultrapure water.

Table 7 shows the results of the ion dissolution validation experiment. All detected elements had concentrations below the instrument’s lower limits, indicating no significant ion dissolution across the two cycles. The presence of Ni and Mo in ultrapure water was attributed to the fact that fluorocarbon resin did not provide a complete seal of the matrix. This suggests that the coating is biofriendly.

Table 7. Verification results of ion dissolution of coating.

Test Time (Day)	Ni $\mu\text{g/L}$	Ti $\mu\text{g/L}$	Mo $\mu\text{g/L}$	Fe mg/L	Mn mg/L	Al mg/L	Cr mg/L
Coating (1–7)	<0.06	<0.46	<0.06	<0.02	<0.004	<0.07	<0.03
Water (1–7)	<0.06	<0.46	<0.06	<0.02	<0.004	<0.07	<0.03
Coating (8–14)	<0.06	<0.46	<0.06	<0.02	<0.004	<0.07	<0.03
Water (8–14)	<0.06	<0.46	<0.06	<0.02	<0.004	<0.07	<0.03

4. Conclusions

In this study, an $\text{Al}_2\text{O}_3\text{-40TiO}_2$ ceramic coating was deposited on 20MnNiCr steel via the atmospheric plasma spraying (APS) method. The corrosion behaviors of the coating were studied in artificial seawater, as well as in a simulated deep-sea environment with hydrogen sulfide and high pressure, aiming to explore the application prospect of the developed ceramic coating to protect combustible ice mining facilities against corrosion. Ion dissolution experiments were conducted to assess the bio-friendliness of the coating. The following conclusions are drawn based on the results:

- (1) In artificial seawater, the corrosion rate (based on the corrosion current) of the coating first decreased and then increased. It was speculated that the blocking of corrosion products in defect channels, such as pores and cracks, was helpful in delaying the progress of corrosion in the early stage. The dissolution of corrosion products accelerated the corrosion rate in the later stage. The coating had a corrosion current in the order of $10^{-6} \text{ A}\cdot\text{cm}^{-2}$ in artificial seawater, implying good protection in conventional seawater environments;
- (2) In the simulated high-pressure seawater environment with wet hydrogen sulfide, the corrosion rate of the $\text{Al}_2\text{O}_3\text{-40TiO}_2$ coating showed a continuously declining trend. A minimal corrosion rate of 0.0030 mm/a was obtained after the coating was immersed for 30 days. We speculated that corrosion products in the simulated environment, such as metal sulfide, might be more chemically stable than those in artificial seawater, leading to a longer blocking effect. The localized failures of the $\text{Al}_2\text{O}_3\text{-40TiO}_2$ coating were caused by its quality but the coating itself had good corrosion resistance;
- (3) The results of the ion dissolution experiments indicated minimal dissolution of the coated elements after sealing. The validation experiment revealed that the dissolution of non-coated elements, such as nickel and molybdenum, was linked to the fluorocarbon resin layer. The coating material exhibited good bio-friendliness.

Author Contributions: X.Z. and Y.W. developed the idea and drafted the content of the manuscript; X.C. (Xiangxiang Chen) and Q.C. conducted the experiments; X.C. (Xiangxiang Chen) analyzed the data and results and wrote the manuscript; X.Z., Y.W. and H.Z. revised the manuscript and improved the presentation of both the results and the structure of the sections. This study was conducted under the supervision of X.Z. and X.C. (Xudong Cheng). All authors have read and agreed to the published version of the manuscript.

Funding: This study was funded by the Chinese Academy of Sciences under the Cold Spring Device Preliminary Key Technology Research Project: Analogue Simulation Experiment System Overall Design and Key Technology Research (LQ-GJ-01).

Institutional Review Board Statement: Not applicable.

Informed Consent Statement: Not applicable.

Data Availability Statement: The data presented in this study are available from the corresponding author upon request. The data are not publicly available due to privacy.

Conflicts of Interest: The authors declare no conflicts of interest.

References

1. Zhang, Z.G.; Wang, Y.; Gao, L.F.; Zhang, Y.; Liu, C.S. Marine Gas Hydrates: Future Energy or Environmental Killer? *Energy Procedia* **2012**, *16*, 933–938. [[CrossRef](#)]
2. Chong, Z.R.; Yang, S.H.B.; Babu, P.; Linga, P.; Li, X.S. Review of natural gas hydrates as an energy resource: Prospects and challenges. *Appl. Energy* **2016**, *162*, 1633–1652. [[CrossRef](#)]
3. Peketi, A.; Mazumdar, A.; Sawant, B.; Manaskanya, A.; Zatale, A. Biogeochemistry and trophic structure of a cold seep ecosystem, offshore Krishna-Godavari basin (east coast of India). *Mar. Pet. Geol.* **2022**, *138*, 105542. [[CrossRef](#)]
4. Cordes, E.E.; Bergquist, D.C.; Fisher, C.R. Macro-ecology of gulf of Mexico cold seeps (Review). *Annu. Rev. Mar. Sci.* **2009**, *1*, 143–168. [[CrossRef](#)] [[PubMed](#)]
5. Joseph, R.X.; Vinodhini, S.P.; Beryl, J.R. Anti-corrosion and flame-retardant properties of environmentally benign smart functionalized WS₂/rGO in epoxy coatings for enhanced steel structural protection in natural seawater. *Mater. Today Commun.* **2024**, *38*, 107842. [[CrossRef](#)]
6. Liu, Q.Q.; Li, N.P.; Li, C.M.; Duan, J.J. Fabrication of environmentally friendly superhydrophobic coatings for corrosion protection under simulated conditions of antifreeze solutions for heat-source tower. *Surf. Coat. Technol.* **2023**, *471*, 129878. [[CrossRef](#)]
7. Liu, M.Y.; Li, S.N.; Wang, H.; Jiang, R.J.; Zhou, X. Research progress of environmentally friendly marine antifouling coatings. *Polym. Chem.* **2021**, *12*, 3702–3720. [[CrossRef](#)]
8. Aaishwarika, R.S.; Rakesh, G. Immersion studies of Al₂O₃–13% TiO₂ and Cr₂O₃ coatings on ship hull plate in simulated seawater environment in laboratory. *Mater. Today Proc.* **2022**, *48*, 946–951. [[CrossRef](#)]
9. Xiao, L.Y.; Liu, Q.Q.; Wang, J.; Chen, N.N.; Chen, J.H.; Song, J.L.; Zhang, X.; Xiao, K. Study on corrosion mechanism of Al-Zn coatings in the simulated polluted marine atmosphere. *J. Mater. Res. Technol.* **2023**, *25*, 6446–6458. [[CrossRef](#)]
10. Lin, M.; Xiao, J.K.; Sun, G.D.; Wei, X.L.; Wu, D.L.; Cao, P.; Zhang, C. Microstructure and wear behaviors of Cr₂O₃-Al₂O₃ composite coatings deposited by atmospheric plasma spraying. *Surf. Coat. Technol.* **2022**, *444*, 128619. [[CrossRef](#)]
11. Jia, S.K.; Zou, Y.; Xu, J.Y. Effect of TiO₂ content on properties of Al₂O₃ thermal barrier coatings by plasma spraying. *Trans. Nonferrous Met. Soc. China* **2015**, *25*, 175–183.
12. Toma, F.-L.; Stahr, C.C.; Berger, L.-M.; Saaro, S.; Herrmann, M.; Deska, D.; Michael, G. Corrosion Resistance of APS- and HVOF-Sprayed Coatings in the Al₂O₃-TiO₂ System. *J. Therm. Spray Technol.* **2010**, *19*, 137–147. [[CrossRef](#)]
13. Kumar, D.; Singh, P.; Murtaza, Q.; Walia, R.S. Synergistic effect of Al₂O₃-40%TiO₂ coating on thermal conductivity and corrosion rate of SS 304 substrate. *Sādhanā* **2023**, *48*, 266. [[CrossRef](#)]
14. Jiang, L.H.; Dai, W.W.; Wei, Z.; Huang, Y.F.; Wang, F.X.; Hong, S. The effect of immersion time on corrosion performance of the Al₂O₃-40TiO₂ and WC-10Co-4Cr coatings in 3.5 wt.% NaCl solution. *Surf. Topogr.* **2022**, *10*, 015013. [[CrossRef](#)]
15. Wei, Z.U.; Hong, S.; Wei, Z.; Hu, N.; Ying, G.B.; Wu, Y.P. Comparison on long-term corrosion performance of WC-CoCr and Al₂O₃-TiO₂ ceramic coatings in sulphide-containing 3.5 wt% NaCl solution. *Int. J. Refract. Hard. Met.* **2022**, *107*, 105906. [[CrossRef](#)]
16. Li, J.L.; Liu, Z.D.; Ma, H.R.; Wang, X.Y.; Kong, Y.; Li, Y.; Shen, Y. High-temperature corrosion behavior of C276 alloy, 1.4529 steel and laser-cladding 1.4529 coating under the synergistic action of deposited chloride salt and HCl-containing atmosphere. *Corros. Sci.* **2023**, *222*, 111413. [[CrossRef](#)]
17. Wang, K.L.; Wei, Z.; Wei, Z.Y.; Ying, G.B.; Hong, S. Enhanced corrosion resistance of subsonic plasma sprayed nanostructured Al₂O₃-13TiO₂ coating by ultrasound-assisted sealing. *Ceram. Int.* **2023**, *49*, 13852–13859. [[CrossRef](#)]
18. Andrew, S.M.A. Investigating the anisotropic mechanical properties of plasma sprayed yttria-stabilised zirconia coatings. *Surf. Coat. Technol.* **2014**, *259*, 551–559. [[CrossRef](#)]
19. Kahl, B.A.; Yang, Y.S.; Berndt, C.C.; Ang, A.S.M. Data-Constrained Modelling with multi-energy X-ray computed microtomography to evaluate the porosity of plasma sprayed ceramic coatings. *Surf. Coat. Technol.* **2022**, *436*, 128267. [[CrossRef](#)]
20. Weng, P.X.; Guo, P.; Zheng, Z.H.; Ye, H.; Li, Q. Effects of TiO₂ Contents on Phase and Mechanical Properties of Plasma Sprayed Al₂O₃-TiO₂ Coatings. *Mech. Eng.* **2017**, *41*, 13–19. [[CrossRef](#)]
21. Ozkan, S. Effect of the substrate temperature on properties of plasma sprayed Al₂O₃ coatings. *Mater. Des.* **2005**, *26*, 53–57. [[CrossRef](#)]
22. Wu, J.; Cui, J.P.; Zheng, Q.J.; Zhang, S.D.; Sun, W.H.; Yang, B.J.; Wang, J.Q. Insight into the corrosion evolution of Fe-based amorphous coatings under wet-dry cyclic conditions. *Electrochim. Acta* **2019**, *319*, 966–980. [[CrossRef](#)]
23. Picas, J.A.; Rupérez, E.; Punset, M.; Forn, A. Influence of HVOF spraying parameters on the corrosion resistance of WC-CoCr coatings in strong acidic environment. *Surf. Coat. Technol.* **2013**, *225*, 47–57. [[CrossRef](#)]
24. Guan, F.; Zhai, X.F.; Duan, J.Z.; Zhang, J.; Li, K.; Hou, B.R. Influence of sulfate-reducing bacteria on the corrosion behavior of 5052 aluminum alloy. *Surf. Coat. Technol.* **2017**, *316*, 171–179. [[CrossRef](#)]
25. Liu, C.; Bi, Q.; Leyland, A.; Matthews, A. An electrochemical impedance spectroscopy study of the corrosion behaviour of PVD coated steels in 0.5 N NaCl aqueous solution: Part II. *Corros. Sci.* **2003**, *45*, 1257–1273. [[CrossRef](#)]
26. Ahn, S.H.; Choi, Y.S.; Kim, J.G.; Han, J.G. A study on corrosion resistance characteristics of PVD Cr-N coated steels by electrochemical method. *Surf. Coat. Technol.* **2002**, *150*, 319–326.
27. Verdian, M.M.; Raeissi, K.; Salehi, M. Corrosion performance of HVOF and APS thermally sprayed NiTi intermetallic coatings in 3.5% NaCl solution. *Corros. Sci.* **2010**, *52*, 1052–1059. [[CrossRef](#)]
28. Zhou, J.L.; Kong, D.J. Effects of Ni addition on corrosion behaviors of laser clad FeSiBNi coating in 3.5% NaCl solution. *J. Alloys Compd.* **2019**, *795*, 416–425. [[CrossRef](#)]

29. Qin, Y.J.; Wu, Y.P.; Zhang, J.F.; Hong, S.; Guo, W.M.; Chen, L.Y.; Liu, H. Optimization of the HOVF Spray Parameters by Taguchi Method for High Corrosion-Resistant Fe-Based Coatings (Article). *J. Mater. Eng. Perform.* **2015**, *24*, 2637–2644. [[CrossRef](#)]
30. Zhang, G.A.; Zeng, Y.; Guo, X.P.; Jiang, F.; Shi, D.Y.; Chen, Z.Y. Electrochemical corrosion behavior of carbon steel under dynamic high pressure H₂S/CO₂ environment. *Corros. Sci.* **2012**, *65*, 37–47. [[CrossRef](#)]
31. Wen, X.L.; Bai, P.P.; Luo, B.W.; Zheng, S.; Chen, C.F. Review of recent progress in the study of corrosion products of steels in a hydrogen sulfide environment. *Corros. Sci.* **2018**, *139*, 124–140. [[CrossRef](#)]
32. Wei, S. Kinetics of Iron Carbonate and Iron Sulfide Scale Formation in CO₂/H₂S Corrosion. Ph.D. Thesis, Ohio University, Athens, OH, USA, 2006.
33. Wang, Y.F.; Cheng, G.X.; Wu, W.; Qiao, Q.; Li, Y.; Li, X.F. Effect of pH and chloride on the micro-mechanism of pitting corrosion for high strength pipeline steel in aerated NaCl solutions. *Appl. Surf. Sci.* **2015**, *349*, 746–756. [[CrossRef](#)]
34. Xiong, X.H.; Chen, L.B.; Hu, K.X.; Wang, Z.P.; Zhang, Q.X.; Lei, Y.J. Influence of temperature and chloride ion concentration on the corrosion behavior of Mg–4Al–3Ca–0.5RE alloy. *Mater. Corros.* **2019**, *70*, 1214–1221. [[CrossRef](#)]

Disclaimer/Publisher’s Note: The statements, opinions and data contained in all publications are solely those of the individual author(s) and contributor(s) and not of MDPI and/or the editor(s). MDPI and/or the editor(s) disclaim responsibility for any injury to people or property resulting from any ideas, methods, instructions or products referred to in the content.